1 Extreme reduction: Mantle-derived oxide xenoliths from a hydrogen-rich

2 environment

3

4 Griffin, W.L.[1*], Gain, S.E.M.[1,2], Cámara, F.[3], Bindi, L.[4], Shaw, J.[2], Alard, O.[1], Saunders, M.[2], Huang, J-

5 X.[1], Toledo, V.[5] and O'Reilly, S.Y.[1]

6

[1]ARC Centre of Excellence for Core to Crust Fluid Systems (CCFS) and GEMOC, Earth and

Planetary Sciences, Macquarie University, NSW 2109, Australia; bill.griffin@mq.edu.au

[2] Centre for Microscopy, Characterisation and Analysis, The University of Western Australia, WA

6009, Australia

[3] Dipartimento di Scienze della Terra "Ardito Desio", Università degli Studi di Milano, Via Mangiagalli

34, I-20133 Milano, Italy

[4] Dipartimento di Scienze della Terra, Università di Firenze, Via La Pira 4, I-50121 Florence, Italy

[5] Shefa Gems Ltd., Netanya 4210602, Israel

15

Abstract

17 Coarse-grained xenoliths of hibonite + grossite + Mg-Al-V spinel from Cretaceous

18 pyroclastic rocks on Mt Carmel, N. Israel, and from Sierra de Comechingones,

19 Argentina, include spherules, rods and dense branching structures of native

20 vanadium and V-Al alloys. Microstructures suggest that vanadium melts became

21 immiscible with the host Ca-Al-Mg-Si-O melt, and nucleated as droplets on the

22 surfaces of the oxide phases, principally hibonite. Many extended outward as rods or

23 branching structures as the host oxide crystal grew. The stability of V^0 implies

24 oxygen fugacities ≥9 log units below the Iron-Wustite buffer, suggesting a hydrogen-

25 dominated atmosphere. This is supported by wt%-levels of hydrogen in gasses

26 released by crushing, by Raman spectroscopy, and by the presence of VH_2 among

27 the vanadium balls. The oxide assemblage formed at 1400-1200 °C; the solution of

28 hydrogen in the metal could lower the melting point of vanadium to these

29 temperatures. These assemblages probably resulted from reaction between

30 differentiated mafic melts and mantle-derived $CH_4 + H_2$ fluids near the crust-mantle

31 boundary, and they record the most reducing magmatic conditions yet documented

32 on Earth.

33

34 **Introduction**

35 Vanadium is a mildly incompatible, refractory but lithophile transition element; it also

36 can be mildly siderophile, and may have partitioned into Earth's core at high

37 pressure and low oxygen fugacity (fO_2; Huang et al., 2015). Its valence states

38 normally range from +5 to +2. At 1500°C the V^{5+}/V^{4+} transition occurs at fO_2 5 log

39 units above the Iron-Wustite buffer ($\Delta IW+5$), and the V^{3+}/V^{2+} transition at $\Delta IW-6$;

40 native vanadium (V^0) becomes stable at ca $\Delta IW-9$, an fO_2 similar to the early solar

41 nebula (Grossman et al., 2008). Natural V^0 has been reported previously only from

42 sublimates in volcanic fumaroles (Ostrooumov and Taran, 2016), and in ophiolitic

43 chromitites (Ifandi et al., 2018).

44 Here we describe V^0 and V-Al alloys trapped as melts in hibonite ($CaAl_{12}O_{19}$)

45 and grossite ($CaAl_4O_7$) that crystallized in Cretaceous super-reduced melt-fluid

46 systems in northern Israel (Griffin et al., 2019) and Argentina. Sampling and

47 analytical methods are described in the Supplementary Data.

48

49 **Background**

50 Most of the material described here comprises xenoliths from the pyroclastic

51 ejecta of Cretaceous (99-85 Ma) intraplate basaltic volcanoes exposed on Mt

52 Carmel, in northern Israel (Fig.1; Griffin et al., 2016, 2018a, 2019a, references

53 therein). At least eight of these volcanoes erupted over an area of ca 150 km^2, and

54 their xenoliths provide snapshots of similar melt-fluid systems, sampled at different

55 stages of their evolution. Aggregates of skeletal corundum crystals (Carmel

56 Sapphire[TM]) occur as xenoliths in the tuffs, or re-deposited in nearby alluvial placers,

57 mainly in the Kishon River. Melt pockets trapped within and between the corundum

58 crystals contain mineral assemblages requiring high T (>1450-1200 °C), moderate P

59 (ca 1 GPa) and extremely low fO_2 (see below). Detailed evidence for the natural

60 magmatic (i.e. non-anthropogenic, non-electrostatic) origin of the samples has been

61 presented by Griffin et al. (2019b).

62   Paragenetic studies (Griffin et al., 2018a, 2019; Xiong et al., 2017) suggest

63 that both the low fO_2 and the crystallization of skeletal corundum reflect the

64 interaction of differentiated mafic magmas with CH_4+H_2 at high fluid/melt ratios.

65 These fluid-melt systems were sampled by eruption of the host basalts, but were not

66 directly genetically related to them.

67   The earliest paragenesis in the melt pockets of these xenoliths is corundum +

68 tistarite (Ti_2O_3) + carmeltazite ($ZrAl_2Ti_4O_{11}$; Griffin et al., 2018b) + Mg-Al-Ti spinel in

69 a Ca-Mg-Al-Si-O glass. The crystallization of these Ti^{3+}-bearing phases requires fO_2

70 at least 6 log units below the Iron-Wustite buffer (ΔIW-6; Griffin et al., 2016). The

71 original silicate melts were depleted in Fe and Si by the exsolution of immiscible Fe-

72 Ti-C-Si melts, which also occur abundantly as inclusions in the corundum; these

73 melts crystallized moissanite (SiC), TiB_2, TiN and khamrabaevite (TiC) (Griffin et al.,

74 2016). The metal-silicide melts efficiently scavenged Fe and heavier transition

75 elements, so that no Fe-bearing oxides or silicates are found in the melt pockets.

76 The assemblages described here thus formed from residual melts after extensive

77 crystal fractionation and sequential immiscibility, which enriched the residua in minor

78 elements (REE, Zr, Ti, V, Mn, Sc), Ca and Al. Hibonite first appears late in the

79 crystallization sequence, together with corundum, carmeltazite, Mg-Al spinel, TiN,

80 Fe-Ti silicides, TiC and glass.

81   Coarser-grained (to cm-sized crystals; Fig. 2) intergrowths of hibonite,

82   grossite and spinel, as grains up to 2.5 cm across, also occur in placers of the

83   Kishon and Yoqneam Rivers that drain Mt Carmel. They suggest that hibonite-

84   bearing melts like those trapped in the corundum aggregates evolved even further

85   beneath some volcanic centres. In these xenoliths, V^0 and V-Al alloys occur as

86   spherical, rod-like and branching inclusions, mainly in hibonite.

87   At Mt Carmel, the late crystallization of dmisteinbergite (a polymorph of

88   anorthite) in the melt pockets reflects the peritectic reaction Liq + Crn $\rightarrow$ An,

89   equivalent to the incongruent melting of anorthite (An $\rightarrow$ Liq + Crn). This well-studied

90   reaction is experimentally constrained to pressures (P) >0.9 GPa and temperatures

91   (T) of ca 1450 °C (Goldsmith, 1980). Thermodynamic modelling in the CaO-Al_2O_3-

92   SiO_2 system (Ottonello et al., 2013) suggests that grossite may not be stable at P >1

93   GPa. The same modelling shows that the melt-pocket glasses, which clearly were

94   crystallizing corundum (Griffin et al., 2016, 2018a), cannot be in equilibrium with

95   corundum at P <1 GPa. These P-T estimates place the proposed site of fluid-melt

96   interaction in the uppermost mantle; the crust-mantle boundary in the area has been

97   geophysically defined at 20-25 km depth (Segev and Rybakov, 2011). Comparisons

98   of mineral parageneses in the melt pockets with experimental studies suggest that T

99   decreased from >1450°C to ca 1200°C as fO$_2$ dropped from ΔIW-6 to ΔIW≤-9 (Griffin

100   et al., 2018a, 2019a; references therein).

101   We also describe very similar assemblages have been found in an as-yet

102   undocumented locality in the Sierra de Comechingones, Argentina. These samples,

103   obtained from mineral collectors, probably have been taken from similar basaltic

104   cones known to exist in the area.

105

Petrography

The petrography and parageneses of the coarse intergrowths from Mt Carmel are described in detail elsewhere (Griffin et al., 2019a). Resorbed remnants of corundum in hibonite (Mt Carmel) document the peritectic reaction Crn + Liq → Hbn. The latest paragenesis (Fig. 3a) is grossite + spinel + krotite ($CaAl_2O_4$) + fluorite ± the undescribed oxyfluoride phase $Ca_4Al_6F_2O_{12}$ ± fluorine-rich perovskite ($CaTi(O,F)_3$). The Argentinian samples comprise platy cm-sized crystals of V-rich hibonite, in a matrix of grossite, dellagiustaite ($Al_2V^{2+}O_4$ spinel, Cámara et al. 2018), and other phases including $Ca_4Al_6F_2O_{12}$ (Figs 3b,c).

In the Mt Carmel xenoliths, V^0 occurs mainly as spheroidal to amoeboid balls up to mm size in hibonite crystals; some balls show exsolution of Al-rich *vs* Mn-rich vanadium alloys. More commonly, V^0 forms droplets on (0001) planes, or rods normal to (0001); these rods commonly are necked down to produce linear trains of droplets normal to (0001) (Fig 3a). The inclusions are zonally distributed in some crystals (Fig. 4). In the Sierra de Comechingones samples, V^0 forms elongate inclusions in hibonite, normal to (0001), necked down at irregular intervals; some are partially empty (Fig. 5; Fig. SD1). Spheroidal to amoeboid rods up to 0.1-0.2 mm across are mantled by dellagiustaite or V^{3+}/V^{2+}-dominant spinel (Fig. 6). Some examples contain tiny precipitates of Cu, and larger inclusions (Figs 6b,c) can be vesicular, attesting to the presence of volatiles.

In the Mt Carmel material, some spherical V^0 inclusions develop into "dense branching structures" (DBS; Goldenfeld, 1989) that grew roughly normal to (0001) of the host hibonite crystal (Fig. 7; Fig. SD2); each filament terminates in a single euhedral crystal, showing that growth took place in contact with melt. Clusters of fine branches terminate at planes parallel to (0001), suggesting pauses in the growth

131 of the hibonite crystal. Some branches continued to grow when crystal growth

132 resumed, but new droplets of V^0 also nucleated on the new crystal plane and grew

133 independently of the older branches. In the example shown in Fig. 7, this stop-start

134 process occurred at least four times. The 3D-μCT images (Fig. SD2) show that the

135 outer parts of many filaments contain no solid phases, even where they terminate

136 below the present crystal face. These "empty" portions are continuous with the

137 vanadium-filled branches, and make up approximately 3% of the total volume of the

138 branching structures. In the Mt Carmel material, small bulbous protuberances on the

139 sides of some spheroidal V^0 inclusions enclosed in grossite consist of VH_2, the first

140 reported natural metal hydride (Bindi et al., 2019).

141

142 **Mineral Chemistry**

143   The smallest V^0 inclusions in hibonite from Mt Carmel contain 0.5-2.0% Si and

144 1.5-2.5% Mn (the oxide matrix contains no Si). Most larger inclusions have less Si,

145 1-2% Cr, 0.5-3.5% Mn, and up to *ca* 4 wt% Al; irregular balls included in grossite are

146 the latest to form, and contain up to 15 wt% Al (Table 1). Many of the EMP analyses

147 total <100%, which may reflect H in solid solution (see below). The discovery of

148 vanadium dihydride (VH_2; Bindi et al. 2019) among these balls suggests that the

149 deficit could be due to hydrogen in solid solution.

150   EBSD imaging confirms that V^0 in the larger inclusions is cubic, and a TEM

151 diffraction pattern matches the <110> zone axis of V (James and Straumanis, 1960).

152 Three inclusions of Al-rich vanadium analysed by single-crystal XRD have space

153 group *Im*-3*m*, consistent with the Al-V phase diagram (Kroupa et al., 2017). The unit

154 cell increases from 3.032 Å to 3.068 Å as Al increases from ca 2 at.% to >20 at.%

155 (Fig. 8).

156   V^0 in the Sierra de Comechingones hibonite contains almost no Al, but has

157   more Cr than the Mt Carmel examples, and similar Si contents (0.5-2.2 wt%);

158   vanadium-oxide phases analysed by single-crystal XRD yielded either a tetragonal

159   or a monoclinic cell, corresponding to two polymorphs of synthetic $V_{14}O_6\square_8$: a β-

160   phase (space group $I4/mmm$), and a γ-phase (space group $C2/m$) with ordered

161   vacancies. The coexistence of these two phases constrains the temperature to

162   <1350 °C (Davydov and Rempel, 2009). These oxides suggest an fO_2 somewhat

163   higher than in the Mt. Carmel rocks, but the presence of V^{2+} in spinel (dellagiustaite)

164   requires $fO_2 = \Delta IW$ between -6 and -9. Because dellagiustaite rims are found at the

165   interface between V^0 and hibonite and grossite, this texture might represent a later

166   subsolidus high-T diffusion corona formed at higher fO_2.

167

Analysis of included fluids

169   To evaluate the composition of fluids that might be enclosed in the observed

170   voids associated with the vanadium rods and branching structures, four 2-3 mm

171   grains of the hibonite-grossite aggregates and four corundum aggregates from Mt

172   Carmel were analysed for H, C, N, and S contents by ignition in an O_2-He

173   atmosphere at ca 1150 °C, followed by chromatographic analysis (see

174   Supplementary Data). Contents of H, C, S and N are given in Table 2. The hibonite

175   samples contain high concentrations of gas, averaging 1120 ppm C and 2800 ppm

176   H_2 by weight. This is 4-5 times the concentrations found in the corundum

177   aggregates, even though corundum aggregates appear to have more void space

178   than the hibonite crystals. However, in both cases the included fluids are comprised

179   of >95 at.% hydrogen, assuming that oxygen is at most a minor constituent, as

180   consistent with the required low fO_2.

181

Raman Spectroscopy

183   Raman spectra of hibonite from both localities show sharp peaks in the range

184   0-1000 cm^{-1}, indicating that the hibonite is well-crystallized, in contrast to most

185   meteoritic hibonite (e.g. Ma, 2010; Fig. 9). Peak positions agree very well with those

186   observed by Hofmeister et al. (2004) for synthetic hibonite (Table 3). We observe a

187   strong polarization effect on particular Raman shifts. Changes in the Raman shift

188   and intensity of the bands can be ascribed to the small amount of V in the hibonite

189   structure. A broad band at *ca* 1470 cm^{-1} is present only in N-S orientation of the

190   crystals, along with two shoulders at 1256 and 1588 cm^{-1}. These are difficult to

191   attribute, as plausible groups are v_3 modes of CO3 groups, but these are usually

192   very weak in carbonates. Another plausible assignment is to –CH$_2$ and –CH$_3$

193   deformations. In the 3000-4150 cm^{-1} spectral range, we observe (also polarized)

194   Raman shifts corresponding to the stretching of O-H bonds. This implies the

195   presence of H in a nominally anhydrous phase. However, the bonding is not well

196   ordered and the bands are rather broad. Bands are also observed in hibonite from

197   Mt. Carmel but at different Raman shifts. The only mode observed in hibonite from

198   both localities is the Raman shift at *ca* 3950 cm^{-1}, which corresponds to one OH

199   bond with the hydrogen far from any donor oxygen. In the Mt. Carmel hibonite, the

200   band at 3819 cm^{-1} is very strong and this points to a higher content of H diffused

201   within the lattice and defects in the hibonite. This is consistent with the

202   chromatography measurements reported above. The intensity of the bands changes

203   across the crystal, suggesting that the H is related to the degassing of V^0 inclusions,

204   producing voids by volume reduction, as seen in the 3D μ-CT images (Figs SD-1,

205   SD-2), and diffusing the H across the hibonite host.

206

Discussion and Conclusions

208   The structures of the V^0 inclusions (Figs 2-7) clearly suggest the coexistence

209   of an immiscible metallic melt and a low-α_{SiO2} silicate melt that was crystallizing Ca-

210   Al oxides and Mg-Al-V spinel. They are best explained by the nucleation of drops of

211   molten vanadium on the faces of oxide crystals exposed to the silicate melt. Many of

212   these drops apparently attracted more V^0 as the crystal grew, producing larger and

213   elongated inclusions, continuously in contact with the surrounding mixture of

214   immiscible melts. These inclusions are thus analogous in many ways to the CO_2-

215   filled cylindrical inclusions of sulphide melts in clinopyroxene megacrysts from some

216   alkali basalts (Andersen et al., 1987).

217   The dense branching structures (DBS) shown in Figure 7 probably evolved in

218   a different way. They are not crystallographically controlled, but radiate outwards

219   from initial melt droplets (Fig. 7a; Fig. SD2). The formation of such DBS typically

220   reflects diffusion-controlled interface motion such as the growth of a crystal into a

221   fluid under conditions of mild supercooling (Goldenfeld, 1989). Since each branch of

222   the DBS would need to be growing in contact with a fluid, these structures probably

223   grew from the initial ball on a crystal surface, outward into the melt surrounding the

224   hibonite crystal, only to be encased in hibonite as the crystal surface advanced

225   further out into the melt. The obvious planes in Figures 3 and 7b thus could

226   represent stages where the hibonite overgrew and terminated some parts of the

227   expanding DBS, but presented a stable surface for the nucleation of new V^0 droplets.

228   These structures thus reflect an interplay between the growth rates of the V^0 DBS

229   and the hibonite crystal, involving diffusion of several chemical species.

230   Very similar structures, described as "trees" or "cones" have been observed

231   in some high-quality synthetic (HPHT) diamonds grown in metal fluxes (Palynov et

232   al., 1997; Shiryaev et al., 2018); the material in the structures corresponds to Fe

233   alloys or Fe oxides, related to the growth media and/or the sample container. The

234   main differences between these inclusions and the V^0 DBS described here is that

235   many of the branches apparently consist of individual inclusions, and none of the

236   high-quality images provided by Shiryaev et al. (2018) appear to grow from individual

237   larger balls of the metallic material, such as those illustrated in Fig. 7. Both Palynov

238   et al. (1997) and Shiryaev et al. (2018) interpret the structures as bunches of defects

239   related to dislocations in the structure of the host diamond, implying that the metallic

240   phases have nucleated on the defects in a semi-continuous manner as the host

241   crystal grew. In contrast the spherical morphology of most V^0 inclusions described

242   here argues for separation of an immiscible melt, nucleation on the crystal surface

243   and its trapping by the host oxide,

244   However, a defect-related control is plausible in the case of the V^0 inclusions

245   described here. Tiny balls of V^0 appear to have nucleated in abundance on the

246   faces of growing hibonite (and grossite) crystals, but most of those that grow outward

247   form single rods (Fig. 3-5), with atendency to neck down as seen in fluid-inclusion

248   trails in many minerals. The sites of such nucleation may have represented single

249   dislocations or other imperfections. Only a few inclusions have developed into the

250   spectacular DBS shown in Fig. 7; these may have been the sites of more complex

251   dislocation structures, such as subgrain boundaries (Shiryaev et al., 2018).

252   Inclusions of V^0 occur mainly in hibonite, to a lesser extent in grossite and

253   spinel, and rarely in corundum mantled by hibonite; the metallic melt apparently

254   began separating from the parental oxide melt near the temperature of the

255 corundum-hibonite peritectic, driven by a continuing decrease in fO_2 ($V^{2+} \rightarrow V^0$).

256 Vanadium melts at >1900°C, and experimental data in binary systems suggest that

257 the observed levels of Al, Si, Mn and Cr might lower the melting temperature only by

258 <100°C (Table 1a, b). Since the estimated temperature of the Cor +L $\rightarrow$ Hib

259 peritectic is close to 1300°C in the $CaO-Al_2O_3-MgO-SiO_2$ system (de Aza et al.,

260 2000; Jung, 2010), any immiscible V-dominated melt would be expected to freeze

261 upon unmixing, which apparently did not happen.

262   However, the fO_2 required for the presence of a V^0 melt ($\leq \Delta IW$ -9) implies a

263 hydrogen-rich environment, similar to that of the early solar nebula in which hibonite-

264 bearing Calcium-Aluminum Inclusions formed (Grossman et al., 2008). The included

265 gasses (Table 2) are dominated by hydrogen, consistent with the inferred low fO_2,

266 the evidence of hydrogen defects in the Raman spectra of hibonite, and the

267 presence of VH_2 among the V^0 balls (Bindi et al., 2019).

268   In a hydrogen atmosphere, the melting point of vanadium can be lowered by

269 >1000°C as several wt % H_2 dissolves in the melt (Fukai, 2012); solubility increases

270 dramatically with increasing pressure. H_2 is expelled during solidification of the melt,

271 but the solid V^0 phase can retain significant levels of hydrogen in solution to

272 temperatures below 1000 °C. The consistently low analytical totals of the V^0 balls

273 from both localities may reflect this solid solution.

274   The outer portions of many DBS (Mt Carmel), and some rods (Argentina),

275 contain no solid phases, even though the empty branches clearly are continuous

276 with the vanadium-filled ones. Furthermore, some of the larger droplets in the DBS

277 now comprise an irregular lump of V^0 within a subspherical void (Figures 7, SD2).

278 We suggest that these void spaces reflect the exsolution of H_2 from the solidifying V^0

279 (and contracting) melts in the inner parts of the structures. This could lead to the

280   remelting and expulsion of V^0 from the outer parts of the branches, closer to the front

281   of hibonite nucleation, and perhaps to production of the observed VH_2 phase.

282   Similarly, the vesicles observed in some V^0 grains in the hibonites from Sierra de

283   Comechingones (Fig. 5b) may represent the exsolution of H_2 from a cooling melt.

284   The rimming observed around V^0 inclusions in the Argentinian samples could be

285   related to solid-state diffusion of O and Al into V^0, forming both the non-

286   stoichiometric vanadium oxides and the rims of V^{3+}/V^{2+}-dominant spinels, while H_2

287   from former VH_2 inclusions diffused into the hibonite host.

288   The petrographic and paragenetic similarities between the assemblages from

289   Mt Carmel and Sierra de Comechingones strongly suggest similar conditions of

290   formation. At present more constraints are available on the Mt Carmel xenoliths,

291   which apparently crystallized late in the pre-eruption evolution of fO_2 in magma-fluid

292   systems. This evolution ultimately led to the most reducing conditions yet found on

293   Earth, with free hydrogen as the fluid phase. The observed abundance of carbon in

294   the assemblages suggests an important role for CH_4 in this process. At Mt Carmel,

295   such conditions existed for at least 10 m.y. over an area of ca 150 km^2, in the

296   uppermost part of a thin mantle lithosphere, and high fluid/rock ratios would be

297   required to maintain such reduced volumes within the mantle. This suggests the

298   derivation of abundant $CH_4\pm H_2$ fluids from the deeper mantle, which in turn seems to

299   imply that the sublithospheric mantle beneath this area was metal-saturated (i.e. fO_2

300   = IW), such that any C-O-H fluid issuing from it was dominated by $CH_4\pm H_2$. This

301   conclusion has implications for understanding melting and metasomatic processes in

302   the mantle (Griffin et al., 2018).

303   As discussed elsewhere (Xiong et al., 2017; Griffin et al., 2018) there is a

304   significant, if scattered, body of evidence in the published literature that similar

305 reducing conditions may exist elsewhere on Earth, in connection with several types

306 of explosive volcanism. Finally, the Al-rich late-forming V^0 melts reported here

307 represent the first *in situ* observation of Al alloys on Earth, and may add further

308 credence to reports of Al^0 in many other localities (cf. Dekov et al., 2009).

309

Acknowledgements

324

325

References

327 Andersen, T., Griffin, W. L., O'Reilly, S.Y. 1987. Primary sulphide melt inclusions in mantle-

328 derived megacrysts and pyroxenites. Lithos 20, 279-294.

329

330   Bindi, L., Cámara, F., Griffin, W.L., Huang, J-X., Gain, S.E.M., O'Reilly, S.Y. 2019. The

331   discovery of the first natural hydride. Am. Mineral. 104, 611-614.

332

333   Cámara, F., Bindi, L., Pagano, R., Pagano, A., Gain, S.E.M., Griffin, W.L. 2018. Dellagiustaite: a

334   novel natural spinel containing V^{2+}. Minerals 9, 4.

335

336   Davydov, D. A., Rempel, A.A. 2009. Refinement of the V–O phase diagram in the range 25–

337   50 at % oxygen. Inorg. Mat. 45(1), 47–54.

338

339   de Aza, A.H., Iglesias, J.E., Pena, P., de Aza, S. 2000. Ternary system Al_2O_3-MgO-CaO: Part II,

340   Phase relationships in the subsystem Al_2O_3-$MgAl_2O_4$-$CaAl_4O_7$. Jour. Amer. Ceramics

341   Soc. 83, 919-927.

342

343   Dekov, V.M., Arnaudov, V., Munni, F., Borcheva, T.B., Fiore, S. 2009. Native aluminum: does

344   it exist? Am. Mineral. 94, 1283-1286.

345

346   Fukai, Y. 2012. The Metal-Hydrogen System: Basic Bulk Properties. Springer-Verlag, Berlin.

347   355 pp.

348

349   Goldenfeld, N. 1989. Dynamics of dendritic growth. Jour. Power Sources 26, 121-128.

350

351   Goldsmith, J.R. 1980. The melting and breakdown reactions of anorthite at high pressures

352   and temperatures. Am. Mineral. 65(3-4): 272-284.

353

354   Griffin, W.L., Gain, S.E.M., Adams, D.T., Huang, J-X., Saunders, M., Toledo, V., Pearson, N.J.,

355   O'Reilly, S.Y. 2016. First terrestrial occurrence of tistarite (Ti_2O_3): Ultra-low oxygen

356   fugacity in the upper mantle beneath Mt Carmel, Israel. Geology 44, 815-818.

357

358   Griffin, W.L., Huang, J-X., Thomassot, E., Gain, S.E.M., Toledo, V., O'Reilly, S.Y. 2018a. Super-

359   reducing conditions in ancient and modern volcanic systems: Sources and behaviour

360   of carbon-rich fluids in the lithospheric mantle. Mineral. Petrol. 112, Supplement 1,

361   101-114.

362

363   Griffin, W.L., Gain, S.E.M., Bindi, L., Toledo, V., Camara, F., Saunders, M., O'Reilly, S.Y. 2018b.

364   Carmeltazite, $ZrAl_2Ti_4O_{11}$, a new mineral trapped in corundum from volcanic rocks of

365   Mt Carmel, northern Israel. Minerals 8, 601.

366

367   Griffin, W.L., Gain, S.E.M., Huang, J-X., Saunders, M., Shaw, J., Toledo, V., O'Reilly, S.Y.

368   2019a. A terrestrial magmatic hibonite-grossite-vanadium assemblage: desilication

369   and extreme reduction in a volcanic plumbing system, Mt Carmel, Israel. Am.

370   Mineral. 104, 207-219.

371

372   Griffin, W.L., Toledo, V., O'Reilly, S.Y. 2019b. Discussion of "Enigmatic super-reduced phases

373   in corundum from natural rocks: Possible contamination from artificial abrasive

374   materials or metallurgical slags" by Litasov et al. (2019). Lithos (in press).

375

376   Grossman, L., Beckett, J.R., Fedkin, A.V., Simon, S.B., Ciesla, F.J. 2008. Redox conditions in

377   the solar nebula: Observational, experimental and theoretical constraints. In Oxygen

378   in the Solar System (eds. G.J. MacPherson, D.W. Mittlefehldt, J.H. Jones and

379   S.B.Simon), Rev. Mineral. Geochem. 68, 93-140.

380

381 Hofmeister, A.M., Wokenpa, B., Locock, A.J. 2004. Spectroscopy and structure of hibonite,

382   grossite, and $CaAl_2O_4$: Implications for astronomical environments. Geochimica et

383   Cosmochimica Acta 68, 4485-4503.

384

385 Huang, J-H., Huang, F., Evans, L., Glasauer, S. 2015. Vanadium: Global (bio)geochemistry.

386   Chem.Geol. 417, 68-89.

387

388 Ifandi, E., Zaccarini, F., Tsikouras, B., Grammatikopoulos, T., Garuti, G., Karipi, S.,

389   Hatzipanagiotou, K. 2018. First occurrences oF Ni-V-Co phosphides in chromitite

390   from the Agios Stefanos mine, Othrys ophiolite, Greece. Ofioliti 43, 131-145.

391

392 James, W.J., Straumanis, M.E. 1960. Lattice parameter and expansion coefficient of

393   vanadium. Jour. Electr. Soc. 107, 69

394

395 Jung, I-H. 2010. Overview of the applications of thermodynamic databases to steelmaking

396   processes. CALPHAD 34, 332-362.

397

398 Kroupa, A., Mazalova, M., Richter, K.W. 2017. The reassessment of the Al-V system and new

399   assessment of the Al-Si-V system. CALPHAD 59, 47-60.

400

401   Liu, C., Eleish, A., Hystad, G., Golden, J.J., Downs, R.T., Morrison, S.M., Hummer, D.R., Ralph,

402   J.P., Fox, P., Hazen, R.M. 2018. Analysis and visualization of vanadium mineral

403   diversity and distribution. Am. Mineral. 103, 1080-1086.

404

405   Ma, C. 2010. Hibonite-(Fe), $(Fe,Mg)Al_{12}O_{19}$, a new alteration mineral from the Allende

406   meteorite. Am. Mineral. 95, 188-191.

407

408   Ostrooumov, M., Taran, Yu. 2016. Vanadium, V – a new native element mineral from the

409   Colima volcano, State of Colima (Mexico), and implications for fumarole gas

410   composition. Min. Mag. 80, 371-382.

411

412   Ottonello, G., Attene, M., Ameglio, D., Belmonte, D., Zuccolini, M.V., Natali, M. 2013.

413   Thermodynamic investigation of the $CaO–Al_2O_3–SiO_2$ system at high P and T through

414   polymer chemistry and convex-hull techniques. Chem. Geol. 346, 81-92.

415

416   Pal'ynov, Y.N., Khokhryakov, A.F., Borzodov, Y.M., Sokol, A.G., Gusev, V.A., Rylov, G.M.,

417   Sobolev, N.V. 1997.Growth conditions and real structure of synthetic diamond

418   crystals. Russian Geology and Geophysics 38, 920-945.

419

420   Segev, A., Rybakov, M. 2011. History of faulting and magmatism in the Galilee (Israel) and

421   across the Levant continental margin inferred from potential field data. Jour.

422   Geodyn. 51, 264-284.

423   Shiryaev, A.A., Zolotov, D.A., Suprun, O.M., Ivakhnenko, S.A., Averin, A.A., Buzmakov, A.V.,

424   Lysakovskyi, V.V., Dyachkova, I.G., Asadchikov, V.E. 2018. CrystEngComm 20, 7700-

425   7705.

426

427   Xiong, Q., Griffin, W.L., Huang, J-X., Gain, S.E.M., Toledo, V., Pearson, N.J., O'Reilly, S.Y.

428   2017. Super-reduced mineral assemblages in "ophiolitic" chromitites and

429   peridotites: The view from Mt Carmel. Eur. J. Mineral. 29, 557-570.

430

431

432   **Figure Captions**

433

434   Fig. 1. Location maps showing the location of the Mt Carmel volcanic field. (a) Regional

435   setting; box shows Mt Carmel area; (b) Geological map indicating location of Cretaceous

436   volcanic centers.

437

438   Fig. 2. Combined phase map and backscattered electron (BSE) image of typical hibonite-

439   grossite-spinel assemblage from Mt Carmel, with drop-like inclusions of native vanadium

440   (V^0).

441

442   Fig. 3. (a) Transmitted-light photo (plane polars) of hibonite-grossite-spinel aggregate from

443   Mt Carmel, showing inclusions of V^0 in platy hibonite crystals (ca 5 mm across). Note

444   alternating layers with abundant or scarce inclusions, elongation of some inclusions parallel

445   to c-axis, and necking down of inclusions. (b) Hibonite from Sierra de Comechingones, with

446   vanadium rods normal to (0001) in (c) a grossite-$Ca_4Al_6F_2O_{12}$ matrix with skeletal F-rich

447   perovskite and dellagiustaite (V^{3+}/V^{2+} spinel), some rimming $V_{14}O_6$. Each figure is 1.7 mm

448   wide.

449

450   Fig. 4. BSE image of polished section of a hibonite crystal from Mt Carmel (blue prism shows

451   orientation derived from EBSD), with zonal distribution of V^0 inclusions.

452

453   Figure 5. (a) 3D-μCT image of hibonite fragment (length 600 μm) from Sierra de

454   Comechingones, showing necking-down of cylindrical rods of V^0. (b) false-coloured image of

455   (a) showing that some V^0 rods (red) are partially empty (green) and some are rimmed by

456   dellagiustaite.

457

458   Fig. 6. (a) Reflected-light image of a polished rock chip from Sierra de Comechingones,

459   showing a $V_{14}O_6$ inclusion rimmed by dellagiustaite. Red arrow points to a very thin grain of

460      $V^{3+}_{1.78}Al_{0.21}V^{2+}_{1}O_4$; the composition of the dellagiustaite rim is $Al_{1.04}V^{3+}_{0.96}V^{2+}_{0.92}Mg_{0.08}O_4$. (b)

461   BSE image of V^0 inclusion with abundant fluid inclusions (Table 1b, analysis b). (c) BSE image

462   of V^0 inclusion (Table 1b; points 2 and 3 correspond to analyses c and d) with Cu

463   precipitates, rimmed by euhedral Ti-rich dellagiustaite.

464

465   Figure 7. (a) Transmitted-light and BSE images of a spiral dense branching structure of V^0 in

466   hibonite. (b) 3D-μCT image of vanadium DBS in a hibonite crystal from Mt Carmel; each

467   cluster is ca 1 mm high and grows normal to the (0001) face of the hibonite. Red-orange

468   colours show V^0, while green colours represent voids.

469

470   Figure 8. Al content *vs* unit cell dimension of inclusions of Al-bearing vanadium in grossite.

471

472   Figure 9. Raman spectra of hibonite from Sierra de Comechingones and Mt Carmel.

473

474

475

476

477

478

479

480

481

482

483

484   **Table 1.** Mean major-element compositions of vanadium phases, Mt Carmel.

wt%	vanadium		$V_9(Mn,Al)$		V_4Al	
	EMP		EMP		EMP	
	n=5	stdev	n=5	stdev	n=7	stdev
Si	0.42	0.22	0.52	0.11	0.38	0.04
Zr			0.01	0.01		
Ti	0.01	0.02	0.15	0.11	0.20	0.03
Al	0.32	0.5	3.94	1.27	11.58	0.25
Cr	*1.6**		*0.71**		0.44	
V	95.2	3.23	79.83	6.86	83.37	0.76
Fe	0.03	0.01	0.01	0.01		
Mn	1.21	0.63	12.20	6.55	2.09	0.07
Ca	0.09	0.06	0.41	0.35	0.21	0.17
	98.9		97.78		98.28	

   * EDS data

485

486   **Table 2.** Gas analyses of hibonite and corundum aggregates from Mt Carmel.

487

	sample	N [ppm]	C [ppm]	H [ppm]	S [ppm]
hibonite xl	982	**60**	**1041**	**1572**	**73**
hibonite aggregate	982	**41**	**1165**	**2360**	**64.3**

20

hibonite	1124B	**122**	**1165**	**3293**	**113.1**
hibonite	1124B-dup.	**43**	**1196**	**3925**	**228.7**
corundum semi-transparent	1124	**156**	**329**	**554**	**166**
corundum-brecciated	1124	**21**	**152**	**63**	**22.6**
corundum with glass	1124	**26**	**415**	**677**	**115.7**
corundum	1124	**226**	**347**	**667**	**222.5**

488

489

490 **Table 3.** Observed Raman shifts in hibonite from Sierra di Comechingones (Argentina) and

491 Mt. Carmel (Israel)

492

Synthetic (Hofmeister et al. 2004)	Sierra de Comechingones	Sierra de Comechingones	Mt Carmel
Orientation	lath E-W	lath N-S	lath N-S
v (cm^{-1})	v (cm^{-1})	v (cm^{-1})	v (cm^{-1})
		85	**84.3**
			102.1
	130.8	**130.8**	127
193.7			
209.4p	205.4	**205.4**	**208.9**
250.5p			
274.0	268.6	275.8	273.9
331.9	**318.9**	323.7	
	358.3	**345.7**	**349.6**
399.4			
449.5		438	
457.8	457	**453.8**	**451.9**
489.1	485.4	**485.4**	**485.4**
529.5	522	531	534.7
564.5	576.3		
		593.6	
624.5			
640.4		643.7	643.3
683.8	685.6	681.6	**678.9**
	726.3		
741.0	**744.9**		
773.9	**767**		762.6
795.8		804.3	808
837.3		838.	837.4
872.9	**870**	**871.7**	**875.7**
910.0	905.6	909.9	902.4
		3314	
			3437
			3497
	3640	3623	
	3682	3681	

		3819
	3945	3954
		4063

493   *bold = stronger bands

494

495

496

497

498

499   **Appendix.** Sampling and analytical methods

500   *Sampling*

501   The Shefa Yamim exploration project is aimed at the discovery of economically viable

502   placer deposits of gemstones (mainly sapphire, ruby, hibonite, moissanite) and other

503   commodities within the drainage basin of the Kishon River. Over >10 years, the project has

504   sampled the Cretaceous pyroclastic centers on Mt Carmel (Fig. SD1: Rakefet, Har Alon, Bat

505   Shelomo, Muhraka and Beit Oren complexes) and adjacent areas (Ein Ha-Shofet), and minor

506   and major drainages in the Yaz'rael Valley. Samples range in size from several kg to >1000

507   tonnes. All samples were run through a static grizzly screen to remove pieces larger than

508   100mm in diameter. Rock samples from the vents were coarsely crushed and then treated

509   in the same way as alluvial samples. The <100mm fraction was washed in a scrubber that

510   breaks up any clods. The <0.5mm component is suspended in the wash water and pumped

511   to settling ponds; fractions larger than 25 mm are used to backfill exploration pits. Samples

512   in the +8mm-16mm and +16mm-24mm size fractions are sorted by hand on a picking belt.

513   The +0.5 -8mm component of the sample is washed and classified into 5 fractions: 0.5-

514   0.7mm, 0.7-1mm, 1-2mm, 2-4mm, 4-6mm, 6-8mm. These fractions are transferred to a

515   pulsating jig plant for gravity separation. Samples in the 2mm-8mm size fractions are

516   visually inspected after the jigging process and sorted in the recovery laboratory. The three

517   smallest size fractions are jigged separately. The heavy concentrate in the center of the jig

518   pan is collected and dried; material on the outer part of the jig pan is discarded. The sorters

519   in the laboratory have demonstrated their efficiency in identifying and recovering a wide

520   range of mineral species, including garnet (pyrope), ilmenite, spinel, chrome-diopside,

521   diamond, moissanite, sapphire, ruby, Carmel Sapphire™, hibonite, rutile and zircon. The

522   material described here is dominated by samples from the Rakefet Magmatic Complex, and

523   the alluvial deposits of the Kishon River mid-reach, because these localities have been most

524   thoroughly bulk-sampled, providing abundant material.

525   The unprocessed heavy mineral concentrates of several samples were hand-picked

526   under a binocular microscope in the CCFS laboratories. Several rock samples also have been

527   processed by SelFrag (electrostatic disaggregation) techniques at CCFS, sieved and hand-

528   picked after magnetic and heavy-liquid separation.

529

530

531   *Analytical Techniques*

532   *SEM, EMP*

533   Samples were mounted in epoxy blocks, polished and coated with carbon. A Zeiss

534   EVO MA15 scanning electron microscope (SEM) at the Geochemical Analysis Unit (GAU),

535   Macquarie University, Sydney, Australia was used to capture Backscattered Electron (BSE)

536   images and Energy Dispersive X-ray spectrometry (EDS) was used to map the elemental

537   composition of the samples, and to analyze phases of interest. An accelerating voltage of 15

538   keV and a beam current of 1 nA was used.

539   Major and minor elements were determined by electron microprobe (EMP) using a

540   CAMECA SX100 equipped with five wavelength-dispersive spectrometers at the Macquarie

541   University GeoAnalytical (MQGA; formerly GAU), Macquarie University, Sydney, Australia.

542   Analyses were performed using a focused beam (1-2 μm) with an accelerating voltage of 15

543   keV and a beam current of 20 nA. Standards were a suite of natural and synthetic minerals.

544   Peak counting varied between 10 – 20 s, and background was counted for 5 – 10 s on either

545   side of the peak. Oxygen and carbon were measured directly; matrix corrections were

546   carried out by the ZAF software.

547   Major and minor elements also were determined by electron microprobe (EMP)

548   using a JEOL 8530F electron microprobe equipped with five wavelength dispersive

549   spectrometers at the Centre for Microscopy Characterisation and Analysis (CMCA), The

550   University of Western Australia, Perth, Australia. Analyses were preformed using a fully

551   focussed beam with an accelerating voltage of 15 keV, a beam current of 15 nA. Standards

552   were a suite of natural and synthetic minerals. On-peak counting times were 30 seconds for

553   all elements. X-ray intensity data was corrected for Time Dependent Intensity (TDI) loss (or

554   gain) using a self-calibrated correction for Si kα, Ti kα, Mn kα, Na kα, K kα and mean atomic

555   number (MAN) background corrections were used throughout (Donovan & Tingle, 1996;

556   Donovan et al., 2016). Unknown and standard intensities were corrected for deadtime.

557   Oxygen was measured, matrix corrections and ZAF correction were applied throughout.

558

559   *Transmission Electron Microscopy*

560   FIB foils from the region of interest were prepared for TEM using a dual-beam FIB

561   system (FEI Nova NanoLab 200). High Angle Annular Dark Field Scanning Transmission

562   Electron Microscopy (HAADF-STEM) imaging and element mapping were carried out using

563   an FEI Titan G2 80-200 TEM/STEM with ChemiSTEM Technology operating at 200 kV at the

564   Centre for Microscopy Characterisation and Analysis (CMCA), The University of Western

565   Australia, Perth, Australia. The element maps were obtained by energy dispersive X-ray

566   spectroscopy using the Super-X detector on the Titan with a probe size ~1 nm and a probe

567   current of ~0.25 nA. Total acquisition times of 20-30 minutes were used to obtain good

568   signal-to-noise ratios. Electron diffraction was carried out using a field limiting aperture that

569   selected an area approximately 400nm in diameter.

570

571   *3D-μCT*

572   X-ray micro-computed tomography (μCT) of Mt Carmel samples was done at the

573   CMCA, Perth. The grain was mounted on a finger of rigid PVC plastic with double-sided tape

574   and a separate tomogram was collected for each grain using a μCT system (Versa 520 XRM,

575   Zeiss) running Scout and Scan software (v11.1.5707.17179, Zeiss). Samples were scanned at

576   50 kV and 77 μA with the source detector positions set to -17.7 and 117 mm, respectively.

577   An LE1 source filter was applied to screen out low energy X-rays. A 0.4X objective lens was

578   used together with 2x camera binning to achieve an isotropic voxel resolution of 9 μm. Each

579   scan comprised 2501 projections through 360o with an exposure of 3s for each projection.

580   Raw data were reconstructed using XMReconstructor software (v11.1.5707.17179, Zeiss)

581   following a standard centre shift and beam hardening correction. The standard 0.7 kernel

582   size recon filter setting was also used. The visualization and analysis of data generated from

583   μCT scans were performed using Avizo (v8.1.1, FEI) software.

584   Micro-CT images of hibonite from Sierra de Comechingones were obtained with a

585   Skyscan1172, Bruker micro CT, with a pixel size of 2.90 μm and a X-ray source at 74 KV and

586   133 μA and an Al-foil of 0.125 mm as a filter. Object to source distance was 46.2 mm and

587 camera to source distance was 276.56 mm. Raw data were reconstructed using CTVox

588 volume rendering software from Bluescientific

589

590 *Released-Gas Analysis*

591 H, C, N, and S contents were obtained using a vario EL cube elemental analyzer

592 (Elementar, Langenselbold, Germany). Aliquots of finely powdered sample, weighing

593 between 80 and 120 mg, were mixed with WO_3 flux (sample:flux ratio between 1/1.2 and

594 1/1.5), packed in Sn-foils, hand pressed, and then ignited in an O_2–He gas atmosphere

595 furnace at around 1150 °C. The produced gases were trapped and sequentially released into

596 a set of chromatographic columns for the analysis of N (no trapping), then C, H, and S. Each

597 sample was measured for 9 min, and released gases were sequentially analyzed with a

598 thermal conductivity detector. Reference materials JP-1, BE-N, PM-S and BAM-U110, were

599 repeatedly measured in the same analytical conditions and yielded average values (Table

600 XX) well within error of accepted or published values as tabulated in the GeoReM database

601 (http://georem.mpch-mainz.gwdg.de/).

602 **Table SD-1.** Reference materials for CHNS analyzer.

603

	H TCD	C TCD	N TCD	S TCD	S IR
JP-1 Peridotite massif (JGS)					
n	4	12	14	14	14
Average ($\mu g\ g^{-1}$) $\pm$ SD	3195 $\pm$ 170	763 $\pm$ 82	91 $\pm$ 23	27 $\pm$ 14	26 $\pm$ 7
RSD %	*5*	*11*	*26*	*51*	*27*
BHVO-2 Basalt, Hawaiian Volcanic Observatory (USGS)					
n	5	16	12	12	8
Average ($\mu g\ g^{-1}$)	181 $\pm$ 45	316+60	219 $\pm$ 34	191 $\pm$ 41	179 $\pm$ 42
RSD %	*25*	*19*	*15*	*21*	*23*
PM-S Microgabbros (SARM)					
n	25	26	24	26	22
Average ($\mu g\ g^{-1}$)	689 $\pm$ 70	992+55	154 $\pm$ 38	1128 $\pm$ 51	1165 $\pm$ 119
RSD %	*10*	*6*	*15*	*5*	*10*
BE-N Altered Basalts (SARM)					
n	14	20	17	21	8
Average ($\mu g\ g^{-1}$)	2771 $\pm$ 534	2301 $\pm$ 147	197 $\pm$ 42	301 $\pm$ 37	298 $\pm$ 23
RSD %	19	6	21	12	8
BAM-U110					
n	13	18	18	17	–
Average ($\mu g\ g{-1}$)	12,258 $\pm$ 1758	72,340 $\pm$ 2640	4237 $\pm$ 165	9114 $\pm$ 1082	–
RSD %	14	4	4	12	–

604 *n* denotes the number of measurements performed; average is the arithmetic means of the *n* values

605 measured and SD is the related standard deviation; RSD % is relative standard deviation expressed in

606 %; TCD: Thermal Conductivity Detector; IR: Infra Red detector.

607

608 *Raman Spectroscopy*

609 Raman spectra were collected with and Horiba LabRAM HR Evolution microscope with a

610 Syncerity OE detector, using 532-nm laser the Department of Erath Sciences, University of

611 Milan. Reflected and transmitted light optics were used to select analysis locations. Hibonite

612 from Sierra di Comechingones was studied from a polished thin section. Hibonite from Mt.

613 Carmel was studied using a raw fragment. The analysis was performed using a 100x

614 objective and 600 (500 nm) grating. Laser power was attenuated to 50% of the power. To

615 maximize the signal-to-noise ratio, two spectra were collected using an exposure time of 30

616 s, and then merged together at the end of the acquisition. Spectra were taken at two

617 polarizations at right angles to check for changes in intensity of the raman shifts. The system

618 was calibrated using the 520 cm^{-1} Raman line of metallic silicon. Spectra were processed

619 using LabSpec v.6 (Horiba ®). Peak positions were obtained by fitting Gaussian peaks.

620 Observed peaks are reported in Table 3 and compared with Raman peaks reported by

621 Hofmeister et al. (2004) for synthetic hibonite. Two spectral ranges are reported in Figures

622 3a (50-1000 cm-1) and 3b (3000-4150 cm-1). Raw Raman spectra have been deposited as

623 supplementary material.

624
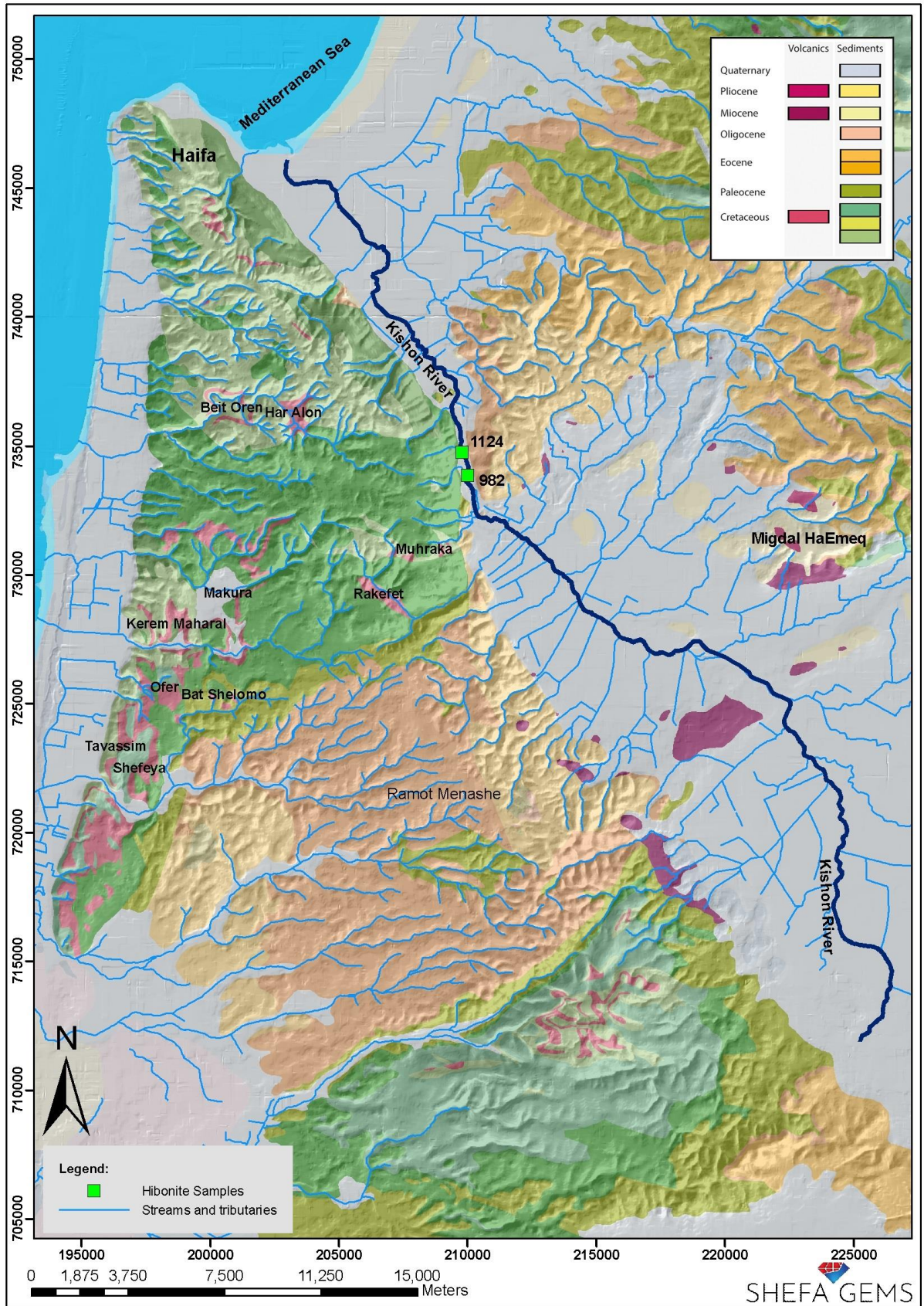
625 **Supplementary Figures**
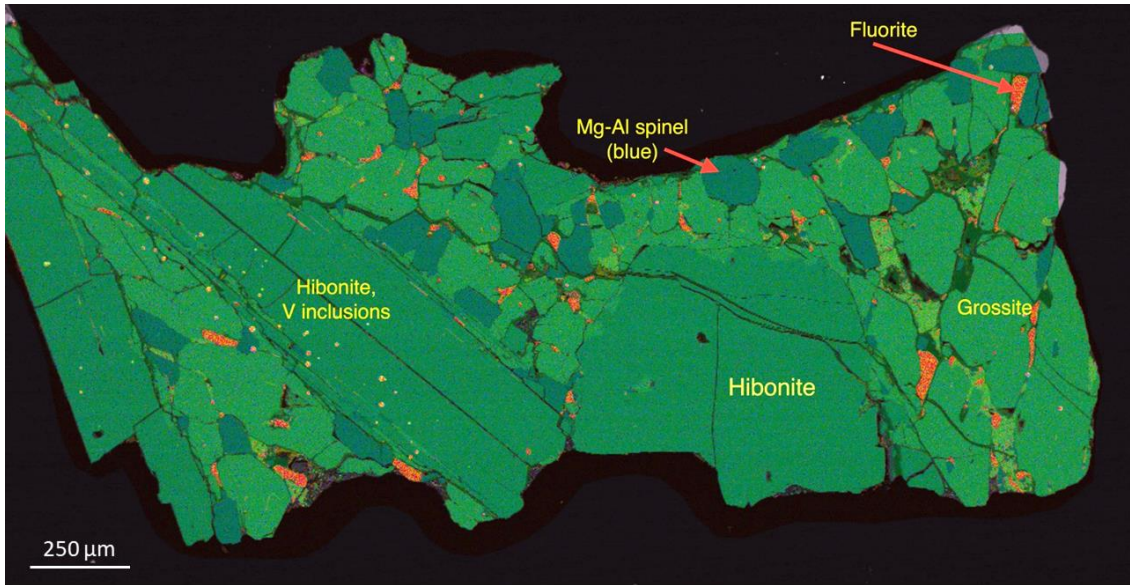
626 Figure SD1. Animated 3D-μCT image of 7b.

627

628 Figure SD2. 3D animation showing successive slices through the structures shown in Figure

629 7b (rotated 90°). Left, grey-scale image; V^0 appears as bright tones, and voids in black.

630 Right, image from Fig. 7b, to show correlation of voids with green colours. Note that some

631 large vanadium "drops" in the middle parts of the structures actually are comprised of voids

632 (green) surrounding an irregular fragment of V^0 (yellow). This is interpreted as the result of

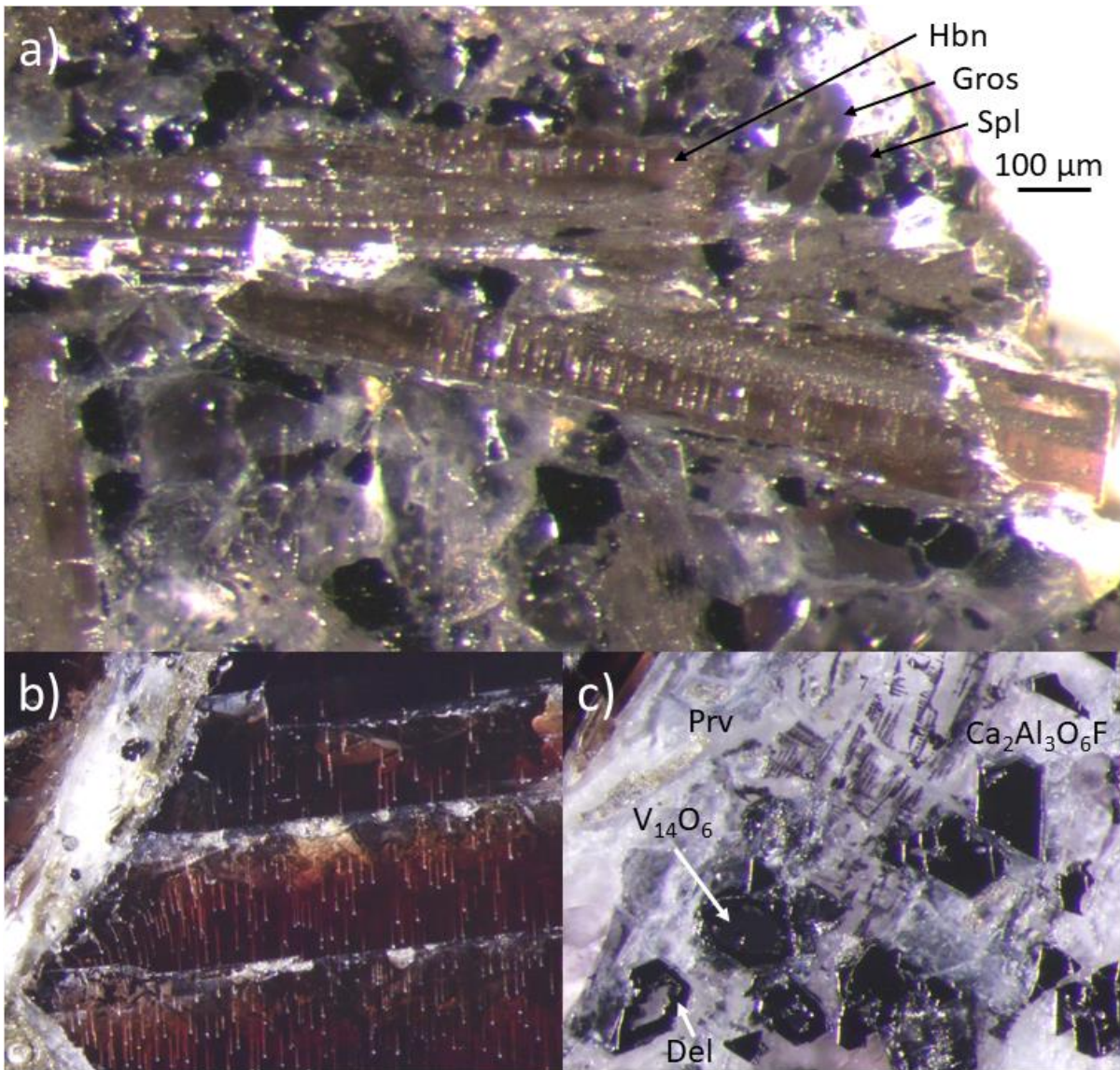633 exsolution of hydrogen from the crystallizing vanadium melt.

634

Figure 1

638

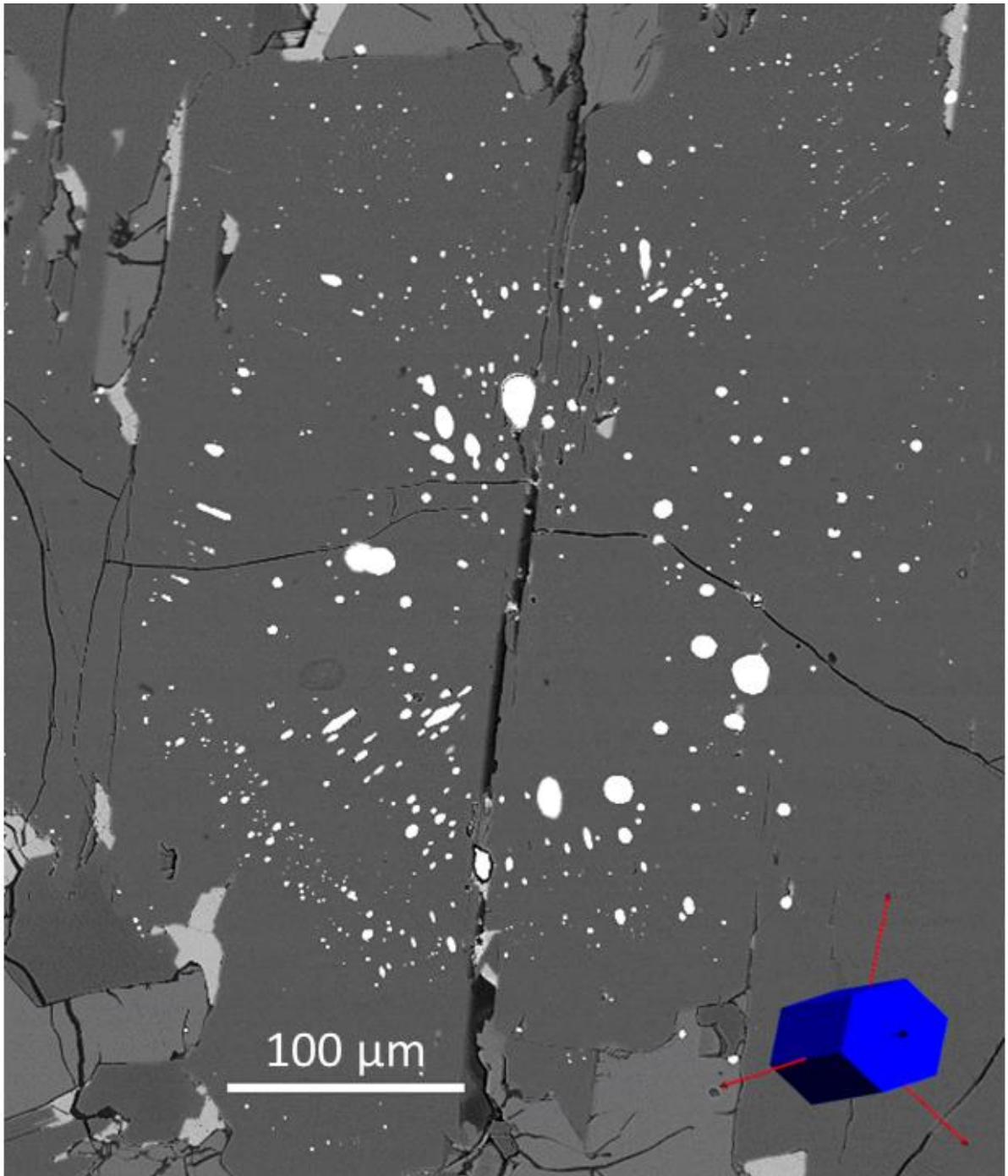639   Figure 2

640

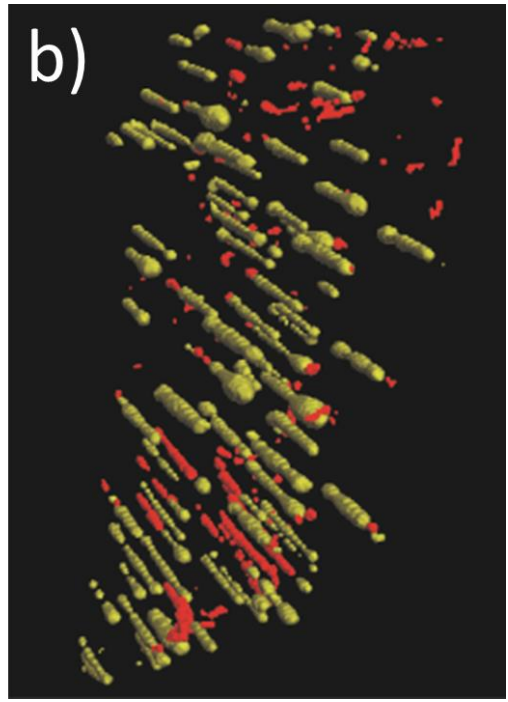641   Figure 3
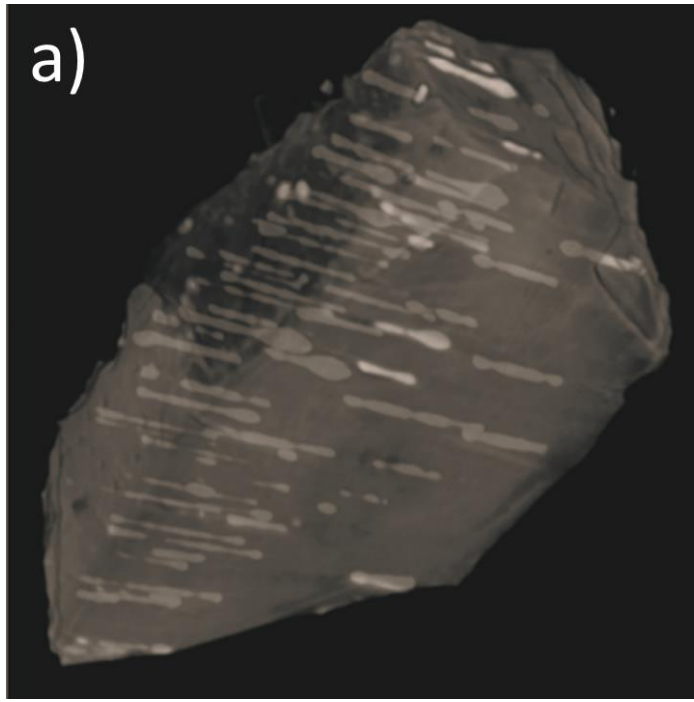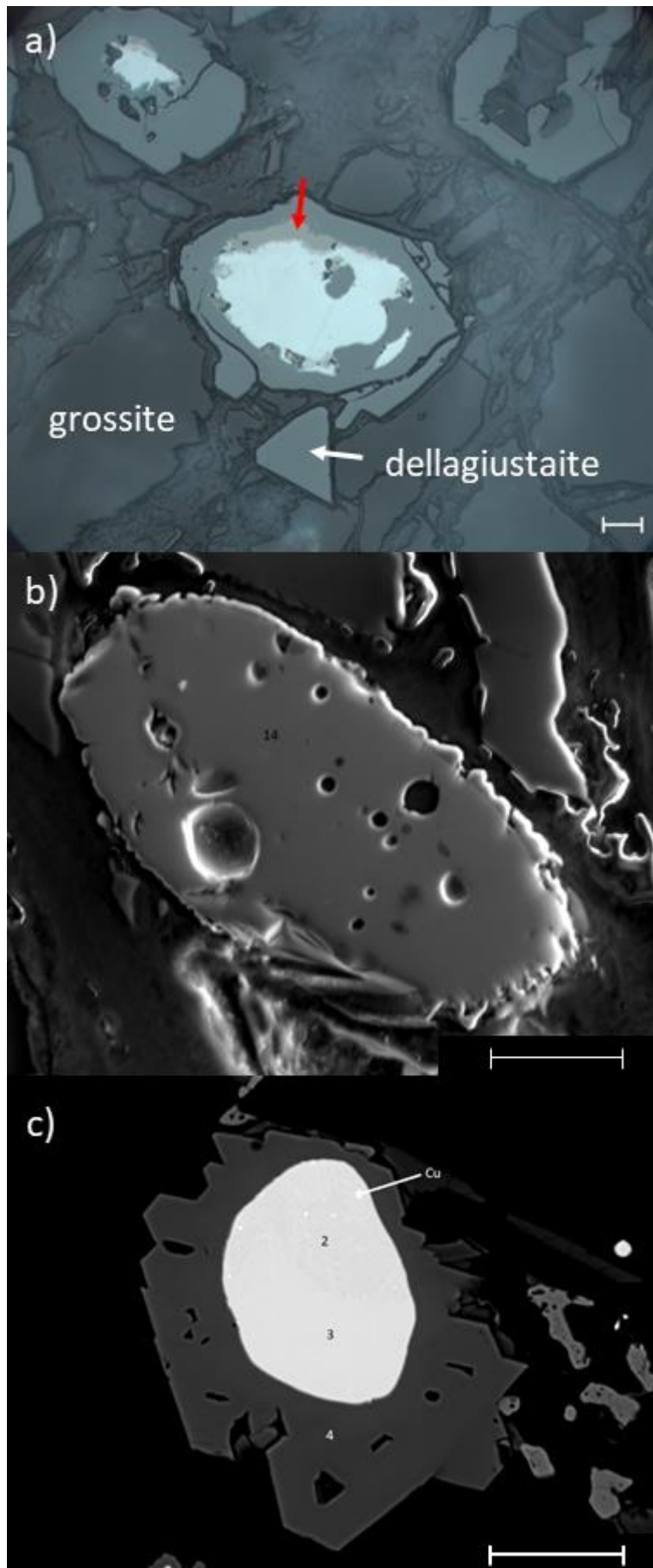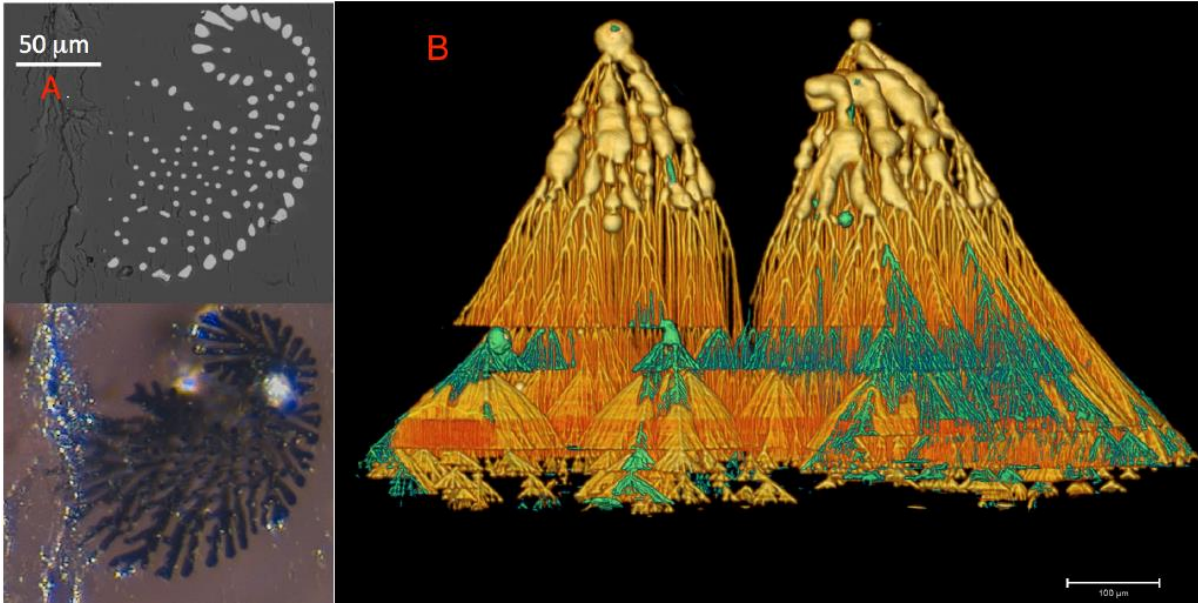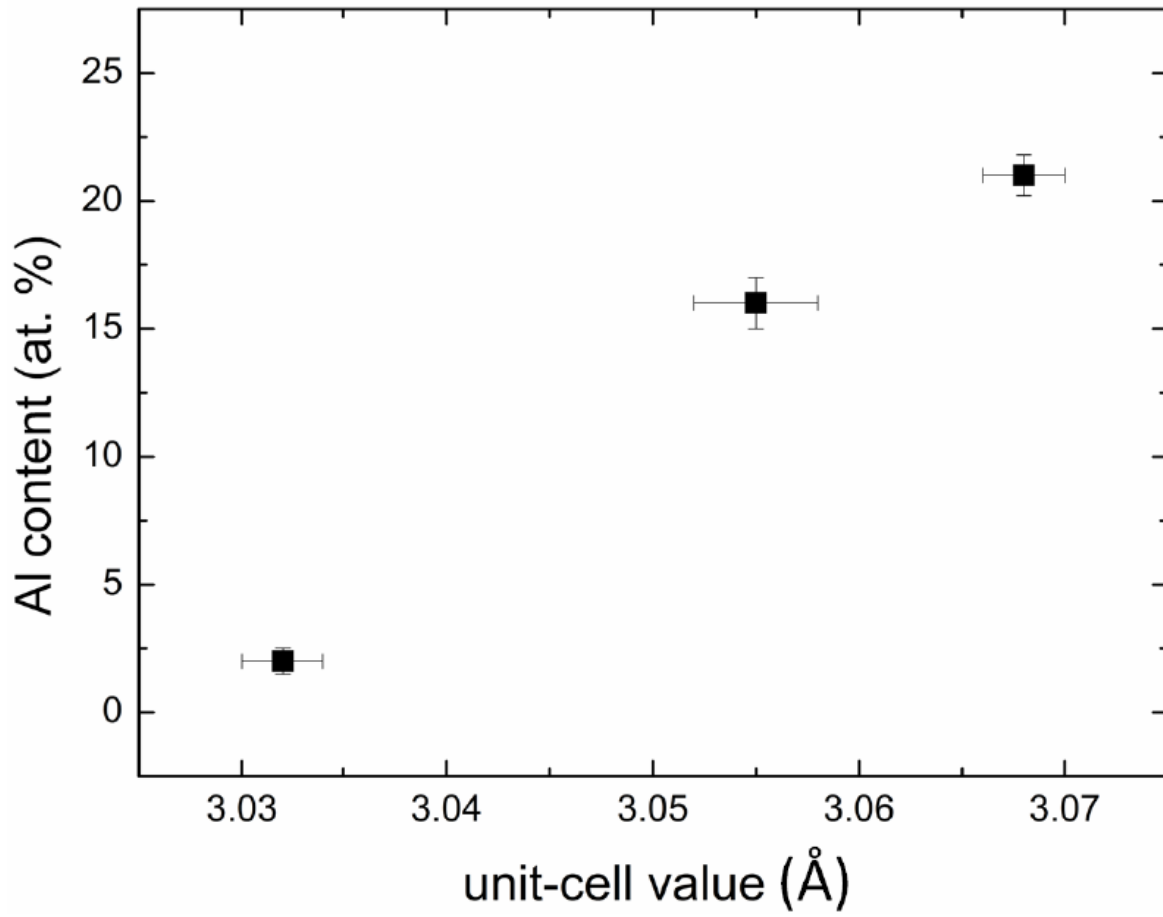
100 μm

642
643   Figure 4
644

645
646 Figure 5
647

a)

grossite

dellagiustaite

b)

c)

Cu

Figure 6

650
651   Figure 7

652
653   Figure 8
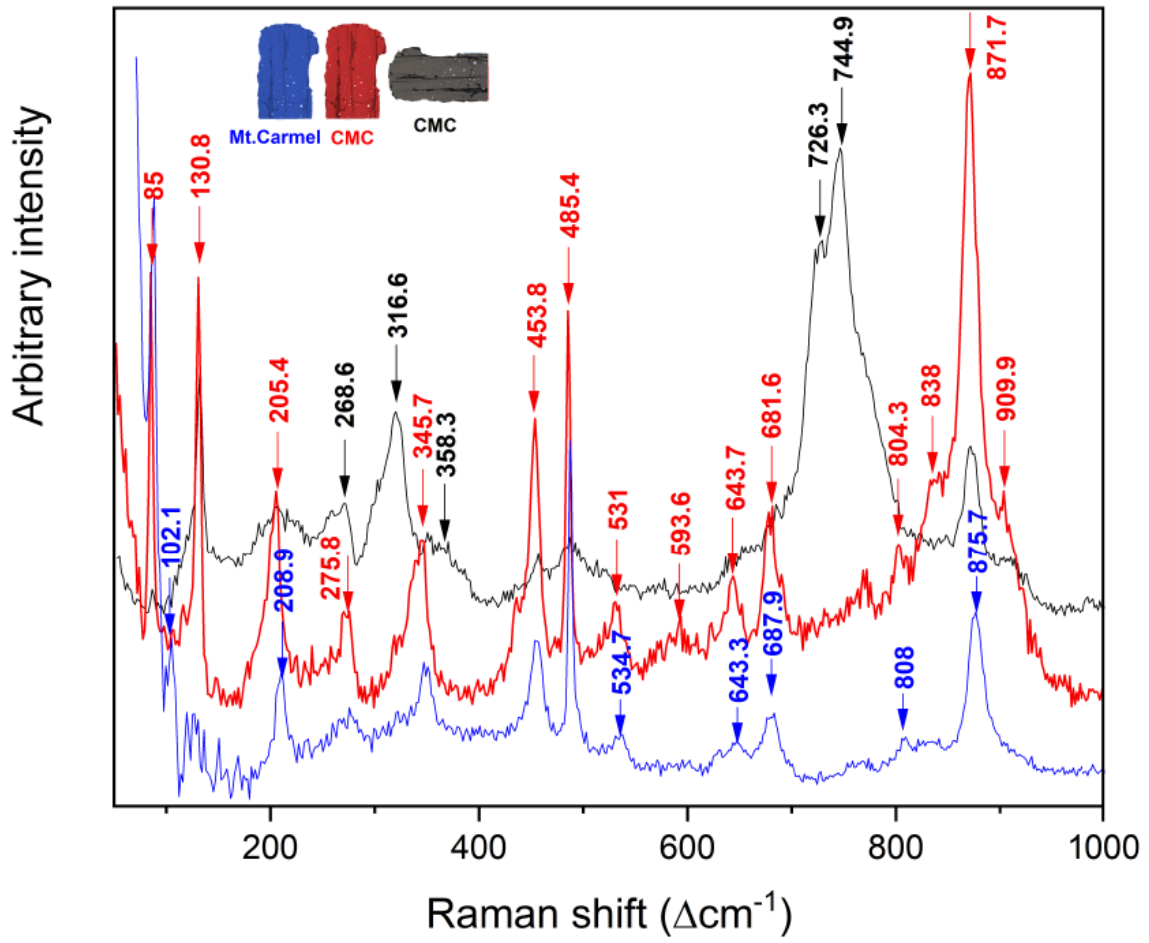
Figure 9

658
659 **Appendix Sampling + Methods**
660
661 **Methods**

662 *Sampling*

663   The Shefa Yamim exploration project is aimed at the discovery of economically viable

664 placer deposits of gemstones (mainly sapphire, ruby, hibonite, moissanite) and other

665 commodities within the drainage basin of the Kishon River. Over >10 years, the project has

666 sampled the Cretaceous pyroclastic centers on Mt Carmel (Fig. SD1: Rakefet, Har Alon, Bat

667 Shelomo, Muhraka and Beit Oren complexes) and adjacent areas (Ein Ha-Shofet), and minor

668 and major drainages in the Yaz'rael Valley. Samples range in size from several kg to >1000

669 tonnes. All samples were run through a static grizzly screen to remove pieces larger than

670 100mm in diameter. Rock samples from the vents were coarsely crushed and then treated

671 in the same way as alluvial samples. The <100mm fraction was washed in a scrubber that

672 breaks up any clods. The <0.5mm component is suspended in the wash water and pumped

673 to settling ponds; fractions larger than 25 mm are used to backfill exploration pits. Samples

674 in the +8mm-16mm and +16mm-24mm size fractions are sorted by hand on a picking belt.

675 The +0.5 -8mm component of the sample is washed and classified into 5 fractions: 0.5-

676 0.7mm, 0.7-1mm, 1-2mm, 2-4mm, 4-6mm, 6-8mm. These fractions are transferred to a

677 pulsating jig plant for gravity separation. Samples in the 2mm-8mm size fractions are

678 visually inspected after the jigging process and sorted in the recovery laboratory. The three

679 smallest size fractions are jigged separately. The heavy concentrate in the center of the jig

680 pan is collected and dried; material on the outer part of the jig pan is discarded. The sorters

681 in the laboratory have demonstrated their efficiency in identifying and recovering a wide

682 range of mineral species, including garnet (pyrope), ilmenite, spinel, chrome-diopside,

683 diamond, moissanite, sapphire, ruby, Carmel Sapphire™, hibonite, rutile and zircon. The

684 material described here is dominated by samples from the Rakefet Magmatic Complex, and

685 the alluvial deposits of the Kishon River mid-reach, because these localities have been most

686 thoroughly bulk-sampled, providing abundant material.

687   The unprocessed heavy mineral concentrates of several samples were hand-picked

688 under a binocular microscope in the CCFS laboratories. Several rock samples also have been

689 processed by SelFrag (electrostatic disaggregation) techniques at CCFS, sieved and hand-

690 picked after magnetic and heavy-liquid separation.

691

692

Analytical Techniques

SEM, EMP

Samples were mounted in epoxy blocks, polished and coated with carbon. A Zeiss EVO MA15 scanning electron microscope (SEM) at the Geochemical Analysis Unit (GAU), Macquarie University, Sydney, Australia was used to capture Backscattered Electron (BSE) images and Energy Dispersive X-ray spectrometry (EDS) was used to map the elemental composition of the samples, and to analyze phases of interest. An accelerating voltage of 15 keV and a beam current of 1 nA was used.

Major and minor elements were determined by electron microprobe (EMP) using a CAMECA SX100 equipped with five wavelength-dispersive spectrometers at the Macquarie University GeoAnalytical (MQGA; formerly GAU), Macquarie University, Sydney, Australia. Analyses were performed using a focused beam (1-2 μm) with an accelerating voltage of 15 keV and a beam current of 20 nA. Standards were a suite of natural and synthetic minerals. Peak counting varied between 10 – 20 s, and background was counted for 5 – 10 s on either side of the peak. Oxygen and carbon were measured directly; matrix corrections were carried out by the ZAF software.

Major and minor elements also were determined by electron microprobe (EMP) using a JEOL 8530F electron microprobe equipped with five wavelength dispersive spectrometers at the Centre for Microscopy Characterisation and Analysis (CMCA), The University of Western Australia, Perth, Australia. Analyses were preformed using a fully focussed beam with an accelerating voltage of 15 keV, a beam current of 15 nA. Standards were a suite of natural and synthetic minerals. On-peak counting times were 30 seconds for all elements. X-ray intensity data was corrected for Time Dependent Intensity (TDI) loss (or gain) using a self-calibrated correction for Si kα, Ti kα, Mn kα, Na kα, K kα and mean atomic number (MAN) background corrections were used throughout (Donovan & Tingle, 1996; Donovan et al., 2016). Unknown and standard intensities were corrected for deadtime. Oxygen was measured, matrix corrections and ZAF correction were applied throughout.

Transmission Electron Microscopy

722   FIB foils from the region of interest were prepared for TEM using a dual-beam FIB

723   system (FEI Nova NanoLab 200). High Angle Annular Dark Field Scanning Transmission

724   Electron Microscopy (HAADF-STEM) imaging and element mapping were carried out using

725   an FEI Titan G2 80-200 TEM/STEM with ChemiSTEM Technology operating at 200 kV at the

726   Centre for Microscopy Characterisation and Analysis (CMCA), The University of Western

727   Australia, Perth, Australia. The element maps were obtained by energy dispersive X-ray

728   spectroscopy using the Super-X detector on the Titan with a probe size ~1 nm and a probe

729   current of ~0.25 nA. Total acquisition times of 20-30 minutes were used to obtain good

730   signal-to-noise ratios. Electron diffraction was carried out using a field limiting aperture that

731   selected an area approximately 400nm in diameter.

732

733   *3D-μCT* *(add method for SdC material)*

734   For X-ray micro-computed tomography (μCT) at the CMCA, the grain was mounted

735   on a finger of rigid PVC plastic with double-sided tape and a separate tomogram was

736   collected for each grain using a μCT system (Versa 520 XRM, Zeiss) running Scout and Scan

737   software (v11.1.5707.17179, Zeiss). Samples were scanned at 50 kV and 77 μA with the

738   source detector positions set to -17.7 and 117 mm, respectively. An LE1 source filter was

739   applied to screen out low energy X-rays. A 0.4X objective lens was used together with 2x

740   camera binning to achieve an isotropic voxel resolution of 9 μm. Each scan comprised 2501

741   projections through 360o with an exposure of 3s for each projection. Raw data were

742   reconstructed using XMReconstructor software (v11.1.5707.17179, Zeiss) following a

743   standard centre shift and beam hardening correction. The standard 0.7 kernel size recon

744   filter setting was also used. The visualization and analysis of data generated from μCT scans

745   were performed using Avizo (v8.1.1, FEI) software.

746

747   *Released-Gas Analysis*

748   H, C, N, and S contents were obtained using a vario EL cube elemental analyzer

749   (Elementar, Langenselbold, Germany). Aliquots of finely powdered sample, weighing

750   between 80 and 120 mg, were mixed with WO_3 flux (sample:flux ratio between 1/1.2 and

751   1/1.5), packed in Sn-foils, hand pressed, and then ignited in an O_2–He gas atmosphere

752   furnace at around 1150 °C. The produced gases were trapped and sequentially released into

753   a set of chromatographic columns for the analysis of N (no trapping), then C, H, and S. Each

754   sample was measured for 9 min, and released gases were sequentially analyzed with a

755   thermal conductivity detector. Reference materials JP-1, BE-N, PM-S and BAM-U110, were

756   repeatedly measured in the same analytical conditions and yielded average values (Table

757   XX) well within error of accepted or published values as tabulated in the GeoReM database

758   (http://georem.mpch-mainz.gwdg.de/).

759   **Table SD-1.** Reference materials for CHNS analyzer.

760

	H TCD	C TCD	N TCD	S TCD	S IR
JP-1 Peridotite massif (JGS)					
n	4	12	14	14	14
Average ($\mu g\ g^{-1}$) $\pm$ SD	3195 ± 170	763 ± 82	91 ± 23	27 ± 14	26 ± 7
RSD %	*5*	*11*	*26*	*51*	*27*
BHVO-2 Basalt, Hawaiian Volcanic Observatory (USGS)					
n	5	16	12	12	8
Average ($\mu g\ g^{-1}$)	181 ± 45	$316 + 60$	219 ± 34	191 ± 41	179 ± 42
RSD %	*25*	*19*	*15*	*21*	*23*
PM-S Microgabbros (SARM)					
n	25	26	24	26	22
Average ($\mu g\ g^{-1}$)	689 ± 70	992 ± 55	154 ± 38	1128 ± 51	1165 ± 119
RSD %	*10*	*6*	*15*	*5*	*10*
BE-N Altered Basalts (SARM)					
n	14	20	17	21	8
Average ($\mu g\ g^{-1}$)	2771 ± 534	2301 ± 147	197 ± 42	301 ± 37	298 ± 23
RSD %	19	6	21	12	8
BAM-U110					
n	13	18	18	17	–
Average ($\mu g\ g{-1}$)	$12,258 \pm 1758$	$72,340 \pm 2640$	4237 ± 165	9114 ± 1082	–
RSD %	14	4	4	12	–

761   *n* denotes the number of measurements performed; average is the arithmetic means of the *n* values

762   measured and SD is the related standard deviation; RSD % is relative standard deviation expressed in

763   %; TCD: Thermal Conductivity Detector; IR: Infra Red detector.

764

765   *Raman Spectroscopy*

766   Raman spectra were collected with and Horiba LabRAM HR Evolution microscope with a

767   Syncerity OE detector, using 532-nm laser the Department of Erath Sciences, University of

768   Milan. Reflected and transmitted light optics were used to select analysis locations. Hibonite

769   from Sierra di Comechingones was studied from a polished thin section. Hibonite from Mt.

770   Carmel was studied using a raw fragment. The analysis was performed using a 100x

771   objective and 600 (500 nm) grating. Laser power was attenuated to 50% of the power To

772   maximize the signal-to-noise ratio, two spectra were collected using an exposure time of 30

773   s, and then merged together at the end of the acquisition. Spectra were taken at two

774 polarizations at right angles to check for changes in intensity of the raman shifts. The system

775 was calibrated using the 520 cm^{-1} Raman line of metallic silicon. Spectra were processed

776 using LabSpec v.6 (Horiba ®). Peak positions were obtained by fitting Gaussian peaks.

777 Observed peaks are reported in Table 3 and compared with Raman peaks reported by

778 Hofmeister et al. (2004) for synthetic hibonite. Two spectral ranges are reported in Figures

779 3a (50-1000 cm-1) and 3b (3000-4150 cm-1). Raw Raman spectra have been deposited as

780 supplementary material.

781

782

783
784